Neurobiology of Disease 141 (2020) 104940

Contents lists available at ScienceDirect

Neurobiology of Disease

journal homepage: www.elsevier.com/locate/ynbdi

ALS and Parkinson's disease genes CHCHD10 and CHCHD2 modify synaptic transcriptomes in human iPSC-derived motor neurons

Sandra Harjuhaahto[a], Tiina S. Rasila[a], Svetlana M. Molchanova[a,b], Rosa Woldegebriel[a], Jouni Kvist[a], Svetlana Konovalova[a], Markus T. Sainio[a], Jana Pennonen[a], Rubén Torregrosa-Muñumer[a], Hazem Ibrahim[a], Timo Otonkoski[a], Tomi Taira[c,d], Emil Ylikallio[a,e], Henna Tyynismaa[a,d,f,*]

[a] Stem Cells and Metabolism Research Program, Faculty of Medicine, University of Helsinki, Helsinki, Finland
[b] Molecular and Integrative Biosciences Research Program, Faculty of Biological and Environmental Sciences, University of Helsinki, Helsinki, Finland
[c] Faculty of Veterinary Medicine, Department of Veterinary Biosciences for Electrophysiology, University of Helsinki, Helsinki, Finland
[d] Neuroscience Center, Helsinki Institute of Life Science, University of Helsinki, Helsinki, Finland
[e] Clinical Neurosciences, Neurology, Helsinki University Hospital, Helsinki, Finland
[f] Department of Medical and Clinical Genetics, University of Helsinki, Helsinki, Finland

ARTICLE INFO

Keywords:
CHCHD2
CHCHD10
Induced pluripotent stem cell
Motor neuron differentiation
CMT2
SMAJ
ALS
Mitochondria
CRISPR/Cas9
RNA sequencing

ABSTRACT

Mitochondrial intermembrane space proteins CHCHD2 and CHCHD10 have roles in motor neuron diseases such as amyotrophic lateral sclerosis, spinal muscular atrophy and axonal neuropathy and in Parkinson's disease. They form a complex of unknown function. Here we address the importance of these two proteins in human motor neurons. We show that gene edited human induced pluripotent stem cells (iPSC) lacking either CHCHD2 or CHCHD10 are viable and can be differentiated into functional motor neurons that fire spontaneous and evoked action potentials. Mitochondria in knockout iPSC and motor neurons sustain ultrastructure but show increased proton leakage and respiration, and reciprocal compensatory increases in CHCHD2 or CHCHD10. Knockout motor neurons have largely overlapping transcriptome profiles compared to isogenic control line, in particular for synaptic gene expression. Our results show that the absence of either CHCHD2 or CHCHD10 alters mitochondrial respiration in human motor neurons, inducing similar compensatory responses. Thus, pathogenic mechanisms may involve loss of synaptic function resulting from defective energy metabolism.

1. Introduction

Mitochondrial intermembrane space proteins CHCHD10 and CHCHD2 of unknown function have gained wide interest after being genetically associated to neurological diseases. Dominant *CHCHD10* mutations underlie motor neuron phenotypes such as amyotrophic lateral sclerosis (ALS), spinal muscular atrophy of Jokela type (SMAJ) and axonal Charcot Marie Tooth disease (CMT2) (Bannwarth et al., 2014; Müller et al., 2014; Auranen et al., 2015; Penttilä et al., 2015) whereas dominant *CHCHD2* mutations cause Parkinson's disease (Funayama et al., 2015). Evidence for whether the mutations cause disease through loss-of-function or toxic gain-of-function has been provided by different studies depending on the model system used (Anderson et al., 2019; Brockmann et al., 2018; Burstein et al., 2018; Genin et al., 2016; Meng et al., 2017).

Human *CHCHD2* and *CHCHD10* originated from a gene duplication event (Cavallaro, 2010). Nuclear genes encode these small CHCH (coiled-coil-helix-coiled-coil helix) domain proteins that are imported into the mitochondrial intermembrane space by the redox-regulated MIA40 pathway (Becker et al., 2012). Both proteins are conserved in metazoans (Longen et al., 2009) but their exact function is unknown. They migrate in the same high molecular weight complex (Burstein et al., 2018; Straub et al., 2018) and have been suggested to form heterodimers (Huang et al., 2018). Studies with overexpression of wild type and mutant CHCHD10 and CHCHD2 proteins, and knockdown and knockout experiments have been reported in various organisms and cultured cells, with different results depending on the mutation, cell type and the gene manipulation method. Effects on mitochondrial ultrastructure, cristae maintenance, or respiratory chain function have been identified in some (Genin et al., 2016; Huang et al., 2018; Meng et al., 2017) but not in all studies (Burstein et al., 2018; Straub et al., 2018). Some studies reported that CHCHD10 is part of the mitochondrial contact site and cristae organizing system (MICOS) (Bannwarth et al., 2014;

* Corresponding author at: Biomedicum Helsinki, r.C525b, Haartmaninkatu 8, 00290 Helsinki, Finland.
E-mail address: henna.tyynismaa@helsinki.fi (H. Tyynismaa).

https://doi.org/10.1016/j.nbd.2020.104940
Received 27 November 2019; Received in revised form 24 March 2020; Accepted 5 May 2020
Available online 11 May 2020

Genin et al., 2016; Zhou et al., 2018), while others did not find evidence for it (Burstein et al., 2018; Huang et al., 2018; Straub et al., 2018). Role as a chaperone for protein import or metal transport has been proposed for CHCHD10 (Burstein et al., 2018), whereas CHCHD2 has been suggested to localize also to the nucleus as a transcription factor for cytochrome *c* oxidase subunit 4 (COX4I2) upon oxidative and hypoxic stress (Aras et al., 2015).

Knockout mice lacking CHCHD2 or CHCHD10 had a normal life span without pathological changes (Anderson et al., 2019; Burstein et al., 2018; Meng et al., 2017). Unexpectedly, knock-in mice with the disease-associated variant p.S59L CHCHD10 developed fatal cardiomyopathy (Anderson et al., 2019; Genin et al., 2019). In the mice, a toxic aggregation model was proposed for pathogenesis where mutant CHCHD10 co-aggregates with CHCHD2 triggering the mitochondrial integrated stress response (Anderson et al., 2019). However, a double knockout mouse model of CHCHD10 and CHCHD2 was recently introduced, which partially phenocopied the mutant S59L mouse phenotype with development of cardiomyopathy (Liu et al., 2019), suggesting that the normal functions of these proteins, and not just aggregates, are also relevant for pathogenesis. Nevertheless, the severe heart phenotypes in mice but not in human patients indicate that CHCHD10/2 biology somewhat differs between human and mice.

Here we generated knockouts of *CHCHD2* or *CHCHD10* in human induced pluripotent stem cells (iPSC). Although CHCHD2 was previously suggested to regulate neuroectodermal differentiation of human embryonic stem cells and iPSC by priming the differentiation potential towards neuroectodermal lineage (Zhu et al., 2016), we show that human iPSC differentiate into functional motor neurons in the absence of CHCHD2 or CHCHD10. However, we found that motor neurons lacking either of these proteins had increased mitochondrial proton leakage, and showed compensatory responses in CHCHD10/CHCHD2 amount, mitochondrial respiration and synaptic transcriptomes. Our results indicate that CHCHD2 or CHCHD10 are not dispensable in human motor neurons.

2. Results

2.1. Human iPSC without CHCHD2 or CHCHD10 are viable and pluripotent

We used CRISPR/Cas9 genome editing to generate knockouts (KO)

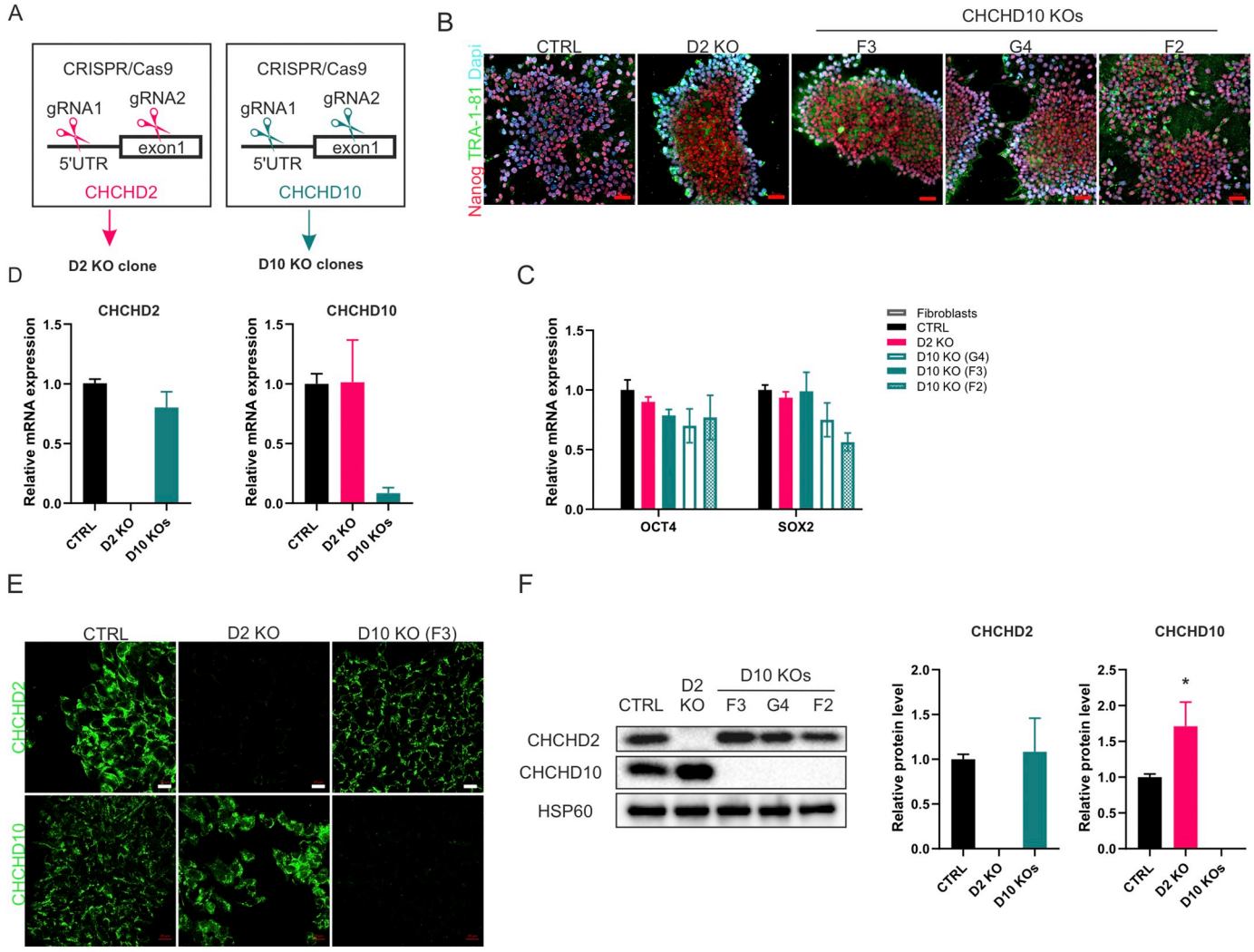

Fig. 1. Human iPSC are viable and pluripotent in absence of CHCHD2 or CHCHD10 (A) Schematic representation of genome editing strategy. CRISPR-Cas9 system was used to target 5′UTR and exon 1. (B) Pluripotency was validated with immunocytochemical analysis of pluripotency markers Nanog and TRA-1-81. Dapi indicates nuclear staining. Scale bar 50 μm. (C) qRT-PCR of pluripotency markers *OCT4* and *SOX2*, normalized to *GAPDH* (n = 3). (D) Expression of *CHCHD2* and *CHCHD10* in knockout iPSCs by qRT-PCR, normalized to *GAPDH* (n = 3 per clone). (E) Immunocytochemical analysis verifies knockout of CHCHD2 and CHCHD10. Scale bar 20 μm. (F) Immunoblot and quantification of CHCHD10 and CHCHD2 levels from whole cell lysates. Quantification shows the average of three independent experiments, normalized to mitochondrial HSP60. Quantifications of D10 KOs clones are shown as pooled results from 3 clones F3, G4 and F2. See also Fig. S1 for results of individual D10KO clones and full immunoblots. Data are shown as mean ± SD, *P < .05.

of *CHCHD2* or *CHCHD10* in human HEL46.11 parental iPSC line (Trokovic et al., 2015) by using two guide RNAs targeted to the 5′ UTR and exon 1 of these genes (Fig. 1A). Four independent KO lines were obtained for *CHCHD10* (D10KO; F3, F2, B9 and G4) and one for *CHCHD2* (D2KO). Pluripotency of KO iPSC lines was verified by immunocytochemistry with Nanog and TRA1-81 antibodies (Fig. 1B) and by the mRNA expression of pluripotency markers *OCT4* and *SOX2* (Fig. 1C). Quantitative PCR showed complete absence of *CHCHD2* mRNA in the D2KO line and absence of *CHCHD10* mRNA in D10KO line G4, but D10KO lines F3 and F2 had 10% of residual *CHCHD10* mRNA expression (Fig. 1D, S1A). Nevertheless, none of the D10KO lines had detectable CHCHD10 protein, and D2KO line had no CHCHD2 protein, as demonstrated by immunostaining (Fig. 1E) and western blotting (Fig. 1F). Quantification of the western blots indicated that CHCHD10 protein level was increased in the D2KO iPSC line in comparison to parental line, whereas D10KO iPSC lines had unchanged CHCHD2 protein levels (Fig. 1F). We also detected higher molecular weight bands in immunoblotting with CHCHD10 and CHCHD2 antibodies that were absent in the corresponding KO cell lines (Fig. S1B and C). Overall, these results suggested that CHCHD2 and CHCHD10 are not essential for iPSC survival.

2.2. Increased mitochondrial proton leak in CHCHD2 and CHCHD10 knockout iPSC

Next, we investigated if the absence of CHCHD2 or CHCHD10 affected mitochondria in iPSC. We performed blue native polyacrylamide gel electrophoresis (BN-PAGE) to detect respiratory chain complexes and found that the overall assembly or the amount of the complexes were not consistently altered (Fig. 2A). Mitochondrial DNA amount in the KO lines was comparable to the parental line (Fig. 2B). Transmission electron micrographs revealed similar mitochondrial ultrastructure in KO iPSC lines as in the parental line (Fig. 2C). Next, we assessed mitochondrial respiration using Seahorse Extracellular Flux Analyzer. We found that the oxygen consumption rate (OCR) differed between parental and KO iPSC lines (Fig. 2D), with the KO showing higher basal (Fig. 2E) and maximal respiration (Fig. 2F) in each KO line compared to the parental line ($p < .0001$). KO lines also had higher ATP-coupled oxygen consumption (Fig. 2G) ($p < .0001$) as measured by inhibition of ATP synthase with oligomycin, which led to smaller decrease in basal respiration in KO iPSC than in parental iPSC. Furthermore, coupling of ATP synthesis to substrate oxidation was reduced in KO iPSC, indicated by increased proton leakage (Fig. 2H) ($p < .0001$). In addition, loss of CHCHD2 or CHCHD10 led to reduced spare capacity, determined from the increase of OCR after addition of uncoupling agent FCCP (Fig. 2I) ($p < .0001$). Ratio between OCR and extracellular acidification rate (ECAR) was systematically increased in the absence of CHCHD2 or CHCHD10, suggesting that KO iPSC utilized the oxidative ATP production more than the parental cells (Fig. 2J) ($p < .0001$). In summary, although we did not observe obvious changes in mitochondrial ultrastructure or respiratory chain complexes in KO iPSC, the increased proton leakage may indicate decreased mitochondrial inner membrane integrity, which is compensated for by increased respiration. Finally, luminescence based measurement of total intracellular content showed similar ATP levels in KO and parental iPSC (Fig. 2K, see also S1D).

2.3. Knockout iPSC differentiate into motor neurons

To investigate if human iPSC can differentiate into spinal motor neurons in the absence of CHCHD10 or CHCHD2, we followed the established differentiation protocol (Guo et al., 2017; Maury et al., 2015) using D2KO and three D10KO iPSC lines together with the parental control line. All lines appeared to differentiate equally well, which we verified for the neuronal differentiation by qRT-PCR of βIII-tubulin (*TUBB3*) and neurofilament medium (*NEFM*) expression (Fig. 3A) and by immunostaining with NEFM, microtubule-associated protein 2 (MAP2) and βIII-tubulin (TUJ1) antibodies (Figs. 3B, S3A). Differentiation towards neuronal lineage was efficient as all DAPI-positive cells were also positive for MAP2 (Fig. 3B) or TUJ1 (Fig. S3). Motor neuronal identity of differentiated neurons was validated by analyzing the expression levels of ISL LIM homeobox 1 (*ISL1*) and choline acetyltransferase (*CHAT*) by qRT-PCR (Fig. 3A), and by immunostaining with ISL1 and motor neuron and pancreas homeobox protein 1 (HB9)/Homeobox protein HB9 antibodies (Fig. 3B). *ISL1* mRNA level was higher in D2KO neurons in comparison to parental line (Fig. 2B), however, we did not observe the same in RNA sequencing of another set of differentiated neurons, showing that loss of CHCHD2 does not consistently lead to increased ISL1. Approximately 50% of DAPI-positive neurons showed pronounced HB9-positivity across all lines in each imaged frame (Fig. 3C). Furthermore, we confirmed by immunostaining that motor neuron markers SMI-32 and ChAT were expressed (Fig. S3B).

Next, we used immunoblotting to detect the levels of CHCHD10 and CHCHD2 in KO motor neurons. We observed a modest increase of CHCHD2 in D10KO motor neurons (Fig. 3D), and a larger increase of CHCHD10 in D2KO motor neurons (Fig. 3D). Higher molecular weight bands that were absent in D10KO iPSCs were again detected by immunoblotting with the CHCHD10 antibody (Fig. S2A), and these were also increased in D2KO neurons. The mRNA expression level of *CHCHD10* was also increased in D2KO neurons and *CHCHD2* expression in D10KO neurons (Fig. 3E). These results showed that human iPSCs differentiate successfully into motor neurons in the absence of CHCHD2 or CHCHD10, with reciprocal compensatory elevation of the two proteins. In particular, the increase of CHCHD10 was evident in CHCHD2 deficiency.

2.4. Knockout motor neurons fire action potentials

To evaluate whether the KO motor neurons were functional and had normal electrophysiological properties, we tested them using whole-cell patch clamp during seventh week of differentiation. Current-clamp mode recordings of iPSC-derived motor neurons demonstrated that all cell lines developed the ability to fire evoked action potentials in response to current injections (Fig. 3F). Many neurons also fired action potentials spontaneously, with similar frequency and amplitude regardless of cell line (Table 1). We found no differences in membrane potential threshold or frequency of firing in response to current injection (Fig. 3G, H). The waveform of individual action potentials was also similar in all cell lines (Table 1). To investigate the Na^+ and K^+ currents in iPSC-derived motor neurons, we applied a series of depolarizing steps while recording in a whole-cell voltage clamp mode (Fig. 3I). No differences in the current-voltage properties of Na^+/Ca^{2+}-currents (Fig. 3K) or K^+ persistent current (Fig. 3J) were observed after normalization to membrane capacitance (pA/pF). This indicated that loss of CHCHD10 or CHCHD2 did not affect excitability of motor neurons. We also evaluated passive membrane properties in voltage clamp mode. Whole-cell capacitance (C_m) values were similar across parental control and knockout iPSC-derived motor neurons, except in D10KO clone G4, which showed a reduction (Table 1). We found no significant differences in the input resistance (R_{in}) of motor neurons. Analysis of passive membrane properties and parameters of action potential firing indicated that iPSC-derived knockout iPSC matured into functional neurons similarly to parental control. This demonstrated that functional motor neuron maturation was not compromised by the loss of CHCHD2 or CHCHD10, and thus these proteins were dispensable for human motor neuron differentiation in vitro.

2.5. Mitochondrial respiration is affected by absence of CHCHD2 or CHCHD10 in human motor neurons

We used transmission electron microscopy to examine how the absence of CHCHD2 or CHCHD10 affected mitochondrial ultrastructure

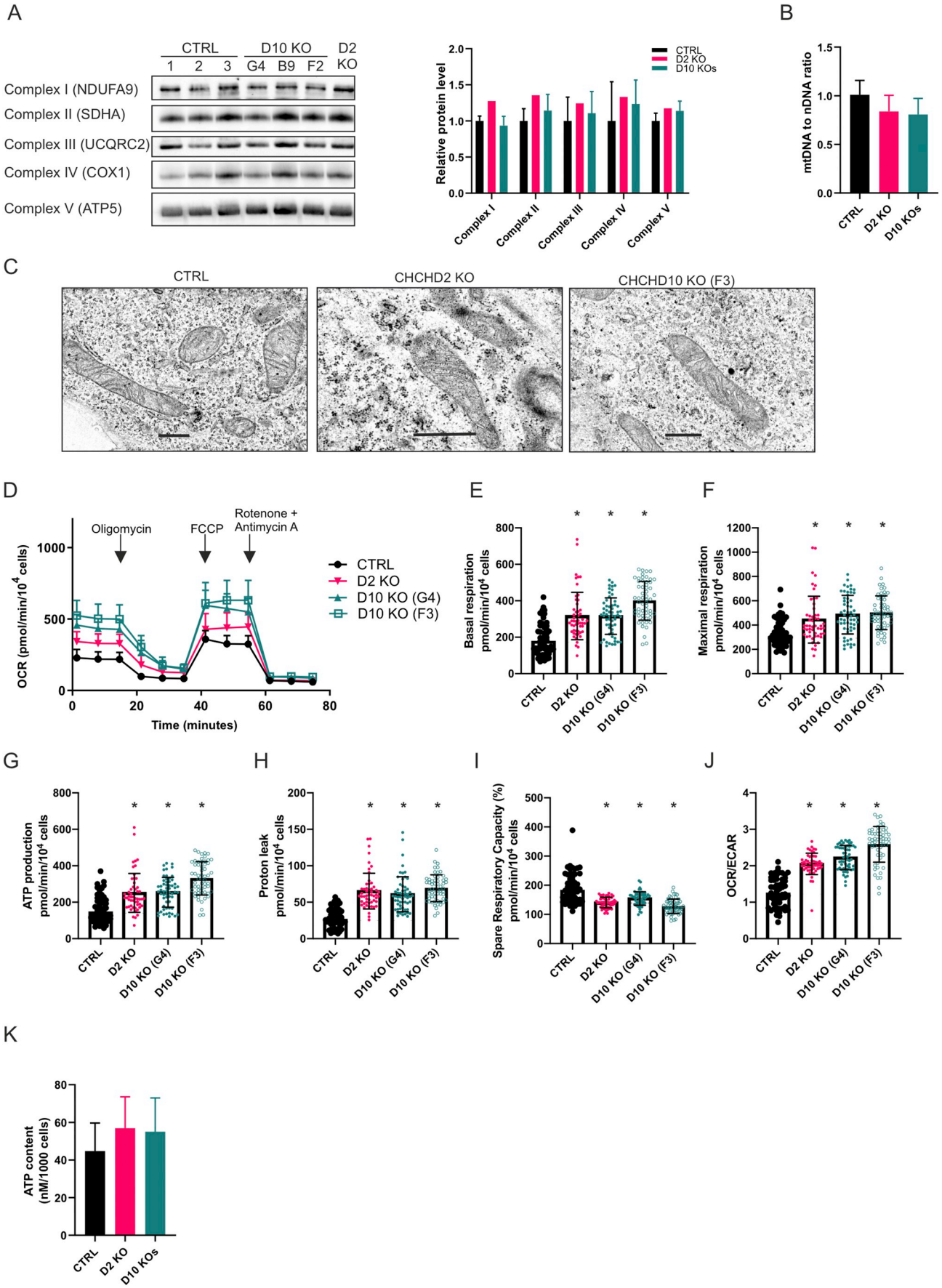

(caption on next page)

Fig. 2. Loss of CHCHD2 or CHCHD10 does not disturb mitochondrial ultrastructure but affects mitochondrial respiration in iPSC. (A) Blue-native PAGE shows unaltered mitochondrial respiratory chain complexes. Quantifications shown relative to average control levels. (B) mtDNA copy number was analyzed by qRT-PCR (n = 3 per clone). (C) Electron micrographs showing intact mitochondrial ultrastructure in CHCHD2 and CHCHD10 knockout iPSC. Scale bar 0.5 μm. (D) Oxygen consumption rate (OCR) measurement in iPSC using Seahorse XF96 Analyzer. Arrows indicate when mitochondrial inhibitors were added (n = 52–58 replicates/cell line from three independent experiments). (E) Basal respiration. (F) Maximal respiration was assessed following mitochondrial uncoupling by FCCP. (G) ATP-coupled respiration was determined after inhibition of ATP synthase by oligomycin. (H) Proton leakage indicates remaining OCR after inhibiting complex I and III by rotenone and antimycin-A. (I) Spare respiratory capacity is determined by the difference between maximal and basal OCR. (J) Ratio between OCR and extracellular acidification rate (ECAR) as an indication of oxidative and glycolytic ATP production, respectively. (K) Total ATP content per 1000 cells. See also Fig. S1C for total ATP results of individual D10 KO clones. Quantifications for D10KO are shown as pooled results from clones F3, G4 and F2. Data are shown as mean ± SD, *P < .05. (For interpretation of the references to colour in this figure legend, the reader is referred to the web version of this article.)

in human neuronal processes. We found abundant mitochondria in all imaged neurites in each cell line, and mitochondrial ultrastructure was similar in KO motor neurons in comparison to the parental control (Fig. 4A). No significant differences in the length of mitochondria between parental control and D2KO or D10KO motor neurons were observed (Fig. 4B). These results indicated that loss of CHCHD2 or CHCHD10 does not affect mitochondrial ultrastructure, abundance or length in human neurites.

Next, we tested if the absence of CHCHD2 or CHCHD10 alters motor neuron bioenergetics. Again, OCR differed between KO and parental motor neurons, although the difference was not as pronounced as in the iPSC (Fig. 4C). The changes were, however, in the same direction as in iPSC, with somewhat higher basal respiration (Fig. 4D) and ATP-coupled oxygen consumption (Fig. 4F), but the increases were not significant in all clones. However, proton leakage was higher in all KO motor neurons in comparison to parental controls (Fig. 4G) ($p < .0001$), whereas spare capacity was reduced (Fig. 4H) ($p < .001$). The ratio between OCR and ECAR was not altered in KO motor neurons (Fig. 4I), which is expected as motor neurons rely much more on oxidative metabolism than iPSC. Overall, these results suggested that CHCHD2 or CHCHD10 are not redundant for mitochondrial respiration in human motor neurons.

2.6. CHCHD10 and CHCHD2 knockout motor neurons have overlapping transcriptome profiles

Next, we assessed whether the loss of CHCHD2 or CHCHD10 had any effect on global gene expression in iPSC-derived motor neurons. We analyzed the mRNA expression of four independent D2KO, four D10KO (G4), four D10KO (F3) and eight parental control motor neuron cultures. Comparison of our parental motor neuron RNA sequencing dataset by principal component analysis (PCA) to available human iPSC-motor neuron datasets (GSE108094 (Rizzo et al., 2019), GSE121069 (Nijssen et al., 2018)) and laser captured post mortem human motor neuron datasets (GSE76220 (Batra et al., 2016), GSE76514 (Nichterwitz et al., 2016), GSE93939 (Allodi et al., 2019)) showed tight clustering of our 8 samples together, supporting consistent, high-quality differentiation conditions of our cultures (Fig. 5A). Interestingly, PCA of our samples showed that the expression profiles of the full D2KO and D10KO motor neurons complete overlapped and were separate from parental control motor neurons (Fig. 5B). Of note, D10KO clone F3, which was a partial knockout having 11% residual *CHCHD10* mRNA expression, showed an intermediate expression profile between full KO (clone G4) and parental control (Fig. S4A), but had consistent differentially expressed genes with the full D10KO (Fig. S4B).

Differential gene expression (DE) analysis by DESeq2 was used to compare full D2KO and D10KO motor neuron transcriptomes to those of parental control. Motor neurons from both KO lines had ~3000 differentially expressed genes (false discovery rate (FDR) < 0.01) compared to parental control motor neurons, and the majority of these changes (> 65%) were shared between the knockouts (Fig. 5C, Table S3). In contrast, only 175 genes were differentially expressed between D2KO and D10KO samples. These results indicated that knockout of either CHCHD2 or CHCHD10 produced similar effects on motor neuron transcriptome.

Among individual genes that were highly and significantly upregulated in both KO motor neurons in comparison to parental control motor neurons were dipeptidyl peptidase like 6 (*DPP6*) ($log_2FC = 3.5$, FDR = 4.4E−103) and Ly6/neurotoxin 1 (*LYNX1*) ($log_2FC = 2.95$ in D2KO and $log_2FC = 2.6$ in D10KO, FDR = 1.5E−259). We validated these findings by qRT-PCR using samples from independent motor neuron cultures (Fig. 5D). We also noted a reduction of transferrin (*TF*) expression in KO motor neurons ($log_2FC = -2.8$ FDR = 2.5E-125).

To identify cellular pathways that were altered by the loss of CHCHD2 or CHCHD10, we used enrichment analysis (Fig. 5E, Table S4). We did not detect enrichment of mitochondria-related pathways, indicating that loss of CHCHD2 or CHCHD10 did not result in transcriptional compensation of mitochondrial functions in human motor neurons. Interestingly, GO term enrichments demonstrated pathways related to neuronal developmental and synapse function, and to ion channel activities, although we had not detected any changes in the ability of the KO motor neurons to fire evoked action potentials. We detected a reduction in several ionotropic glutamate receptor subunits, such as *GRIA1* (AMPA-type receptor subunit), and *GRIK5* (kainate-type receptor subunit), and in NMDA-type glutamate receptor subunits *GRIN2D*, *GRIN3A* and *GRIN3B*, except *GRIN1* that was upregulated. We verified the decrease in *GRIA1* expression in several D10KO clones by qRT-PCR (Fig. 5G). In addition, several metabotropic glutamate receptor subunits, such as *GRM2*, *GRM3*, *GRM4* and *GRM7*, were upregulated (Fig. 5F). In addition, we detected significant changes in the expression of several ion-channel subunits (Fig. S4C). K^+ − channel subunits (*KCNK3*, *KCND2*, *KCNJ3*, *KCNIPA* and *KCNT1*), Na^+ channel subunits (*SCN1A* and *SCN4B*) and Ca^{2+} channel subunits (*CACNG3* and *CACNG8*) were all significantly downregulated. On the contrary, Ca^{2+} channel subunits (*CACNB2*, *CACNA1I* and *CACNA1G*) and Na^+ − channel subunit *SCN1B* were all significantly upregulated (Fig. S4C).

To assess the functional outcomes of reduction of AMPA receptor expression in KO motor neurons, we measured miniature excitatory postsynaptic currents (mEPSCs) by whole-cell patch-clamp in voltage clamp mode (Fig. 5H). In the absence of muscle cells, motor neurons in culture innervate each other with glutamatergic synapses, which we confirmed by recording spontaneous EPSCs in the presence of NBQX, a specific inhibitor of AMPA receptors. In the presence of NBQX, all EPSCs disappeared (data not shown). mEPSCs, recorded in the presence of an inhibitor of action potential firing TTX and a blocker of $GABA_A$ receptors picrotoxin, represent AMPA receptor-mediated currents after spontaneous action potential-independent synaptic release of glutamate. Kinetics of the AMPA receptor-mediated EPSCs were similar in parental control and knockout cell lines (Table 2). The loss of CHCHD2

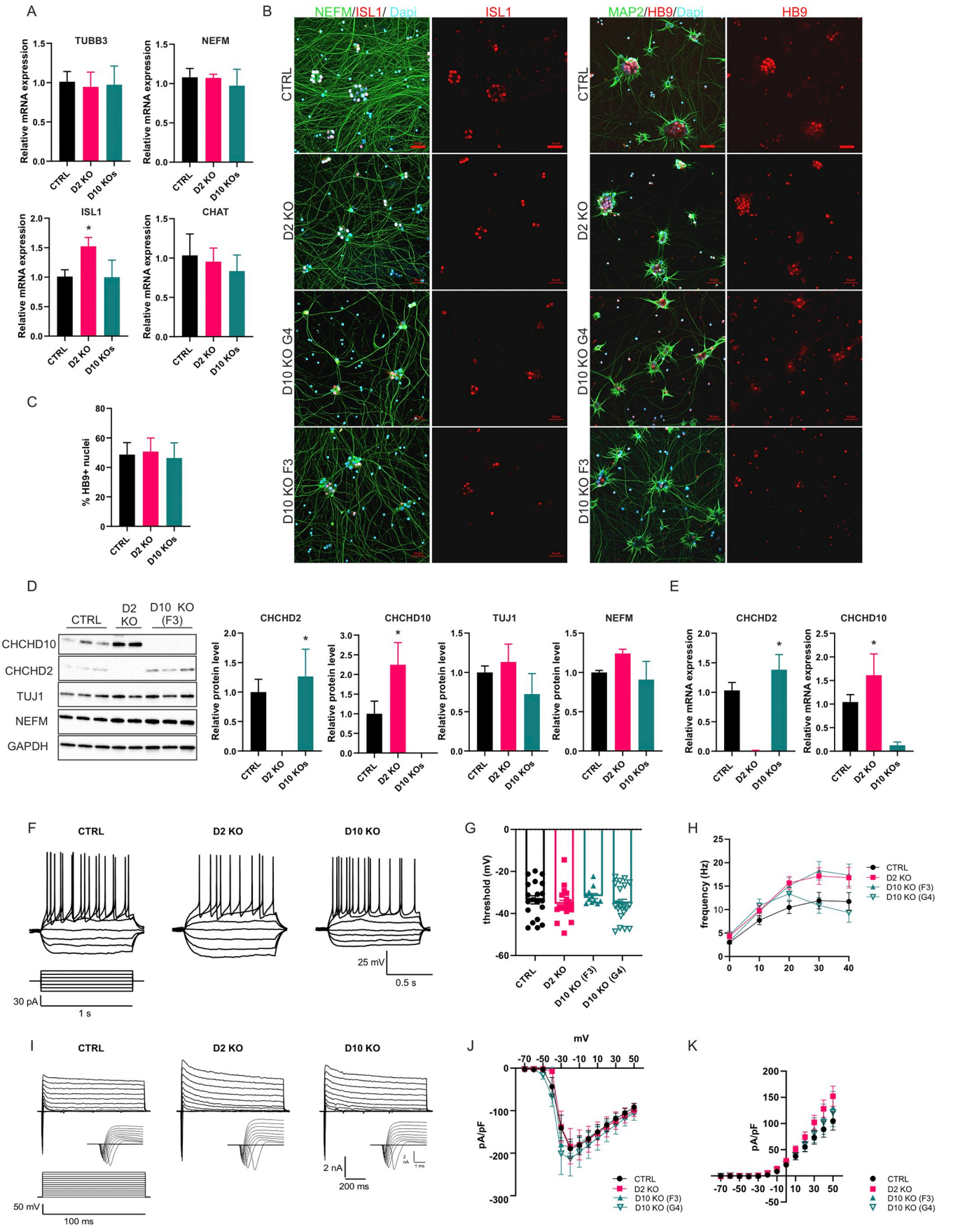

(caption on next page)

Fig. 3. CHCHD2 and CHCHD10 knockout iPSC differentiate into functionally active motor neurons. (A) Validation of the expression of neural transcripts *TUBB3* and *NEFM* and motor neural transcripts *ISL1* and *CHAT* by qRT-PCR, normalized to *GAPDH*, on the day 37 of motor neuron differentiation (n = 3 per clone). (B) Immunocytochemical analysis of ISL1 (red), NEFM (green), MAP2 (green) and HB9 (red) in neuronal cultures. Scale bars 50 μm. Dapi indicates nuclear staining. (C) Manual counting of HB9-positive nuclei in relation to Dapi-positive cells. Total cells counted in 3 frames (n = 52–185 per clone). (D) Immunoblot and quantification of CHCHD2, CHCHD10, TUJ1 and NEFM from whole cell lysates. Quantification shows the results from two or three cultures per clone from two independent experiments, normalized to GAPDH. (E) Expression of *CHCHD2* and *CHCHD10* in knockout iPSC-derived motor neurons by qRT-PCR, normalized to *GAPDH* (n = 3 per clone). (F) Representative traces of evoked action potentials of iPSC-derived motor neurons in response to current injections. (G) Threshold (mV) of action potential firing (n = 11–20 per clone). (H) Action potential firing frequency (Hz) in response to incremental current injections (n = 11–20 per clone). (I) Representative traces of Na^+/Ca^{2+} and K^+ currents, recorded at different membrane potentials. Na^+/Ca^{2+} currents are also shown in inserts, using expanded time scale. (J) Current/voltage relationship characteristics of persistent K^+-current normalized to membrane capacitance (pA/pF) (n = 7–15 per clone). (K) Current/voltage relationship characteristics of Na^+/Ca^{2+} − current normalized to membrane capacitance (pA/pF) (n = 7–15 per clone). Quantifications of D10 KOs clones are shown as pooled results from 3 clones F3, G4 and F2. See also Fig. S2 for full immunoblots. Data are shown as mean ± SD, except mean ± SEM in G-K, *P < .05. (For interpretation of the references to colour in this figure legend, the reader is referred to the web version of this article.)

or CHCHD10 did not alter the amplitude of mEPSCs, which indicates that the quantal size of glutamate release and density of functional APMA receptors were not affected in the KO cell lines.

3. Discussion

The function of CHCHD10 and CHCHD2 proteins and the mechanisms by which the dominant pathogenic mutations in the corresponding genes cause neurological diseases have been under intense research. Studies have suggested that mice lacking CHCHD10 or CHCHD2 develop normally and show no pathologies (Anderson et al., 2019; Burstein et al., 2018; Meng et al., 2017), supporting gain-of-function mechanism for the dominant patient mutations. CHCHD10 knock-in mice carrying a pathogenic patient mutation, however, died of a severe cardiomyopathy (Anderson et al., 2019; Genin et al., 2019), whereas cardiac phenotypes have not been reported in patients (Penttilä et al., 2017). This suggests that besides mice relevant human cell types should be studied for CHCHD10 and CHCHD2 function and defects. Here we utilized iPSC technology that enabled us to address the importance of CHCHD2 and CHCHD10 in human motor neurons, which are affected in CHCHD10-associated phenotypes.

We used CRISPR/Cas9-based gene editing to generate iPSC clones that were lacking either CHCHD2 or CHCHD10, and differentiated those into motor neurons. Knockout motor neurons were compared to neurons differentiated from parental iPSC line that had the identical genome except for the edited gene. Our results showed that iPSC lacking CHCHD2 or CHCHD10 were viable and pluripotent and that CHCHD2 or CHCHD10 were dispensable for human motor neuron differentiation *in vitro*. However, we found that mitochondrial respiration was compromised by loss of either of these two intermembrane space proteins both in iPSC and motor neurons, with compensatory effects.

First, we observed reciprocal compensatory increases in CHCHD10 or CHCHD2 amounts. In particular, CHCHD2 absence was compensated for by CHCHD10 increase in both human iPSC and motor neurons. Also a knockout study in HEK293 cells found reciprocal compensatory responses to loss of either protein (Huang et al., 2018). Compensation may explain why mature motor neurons lacking one of the proteins could be generated. It is, however, possible that double knockout motor neurons would also be functional. We were not successful in generating double knockout iPSC lines in this study and currently are unable to conclude that such iPSC would not be viable. When considering gene therapy options for the dominant CHCHD10/2 mutations, it may be beneficial to know that human motor neurons show reciprocal compensatory responses when the amount of one of the proteins is reduced.

Secondly, although we did not observe changes in mitochondrial ultrastructure in D2KO or D10KO iPSC or motor neurons, mitochondrial proton leakage and respiration were increased in the knockouts. This finding indicates that CHCHD2-CHCHD10 complex is required for efficient mitochondrial respiration, as also suggested by other recent studies (Straub et al. (2018), Burstein et al. (2018) and Xiao et al. (2019)). Increased mitochondrial respiration is likely to be a compensatory effect on less efficient ATP production, caused by increased proton leakage. iPSC are mostly glycolytic (Prigione et al., 2010; Zhang et al., 2011), and thus appeared to have more capacity for compensation than the motor neurons.

Thirdly, although the functionality of cultured knockout motor neurons, as measured by patch-clamp methods, was not affected, D2KO and D10KO motor neurons had largely overlapping transcriptome alterations. In particular, we found an enrichment of genes in synapse function and synaptic membrane pathways. We suggest that these changes are also compensation for the altered mitochondrial function. We detected upregulation of a subset of metabotropic glutamate receptor subunits, whereas ionotropic subunits were mostly downregulated. Expression of *GRIA1*, which encodes the glutamate ionotropic receptor AMPA type subunit 1, was systematically decreased in knockout motor neurons. Differential expression of glutamate receptor subunits could alter synaptic transmission, however, we did not observe any alterations in the amplitude of mEPCSs when comparing KO motor neurons to parental control, indicating that the quantal size of neurotransmitter release or density of postsynaptic receptors was not affected. It is possible that the increased metabotropic subunit expression compensated for the downregulation of *GRIA1*. Even though

Table 1
Passive membrane properties and action potential firing in motor neurons.

	Parental control (n)	D2KO (n)	D10KO F3 (n)	D10 KO G4 (n)
Capacitance, pF	28.8 ± 3.1 (25)	22.0 ± 1.2 (26)	28.1 ± 1.6 (11)	20.5 ± 1.8 (21)*
Input resistance, MΩ	747.8 ± 93.1 (25)	827.0 ± 90.7 (26)	751.7 ± 110.6 (11)	958.2 ± 135.8 (21)
Resting membrane potential, mV	−43.2 ± 2.0 (24)	−41.4 ± 1.7 (22)	−48.0 ± 1.8 (10)	−42.9 ± 1.7 (16)
Spontaneous AP frequency, Hz	2.2 ± 0.4 (18)	2.6 ± 0.5 (13)	1.1 ± 0.3 (8)	2.8 ± 0.6 (14)
Spontaneous AP amplitude, mV	60.0 ± 3.8 (18)	54.5 ± 2.4 (13)	63.4 ± 3.9 (8)	53.4 ± 1.6 (14)
Rheobase, pA	24.8 ± 3.8 (20)	19.0 ± 1.9 (19)	27.3 ± 4.5 (11)	18.5 ± 2.2 (20)
Evoked AP amplitude, mV	59.7 ± 3.2 (20)	58.2 ± 2.9 (19)	56.9 ± 2.1 (11)	59.6 ± 2.3 (20)
Evoked AP half-width, ms	1.4 ± 0.08 (20)	1.3 ± 0.06 (19)	1.2 ± 0.08 (11)	1.2 ± 0.04 (20)
After-hyperpolarization amplitude, mV	17.5 ± 2.1 (20)	15.8 ± 1.6 (19)	18.1 ± 1.1 (11)	16.7 ± 1.7 (20)
After-hyperpolarization decay time, ms	13.0 ± 0.9 (20)	13.2 ± 1.0 (19)	13.5 ± 1.9 (11)	11.5 ± 0.6 (20)

n = number of cells tested. *p < .05 compared to parental control.

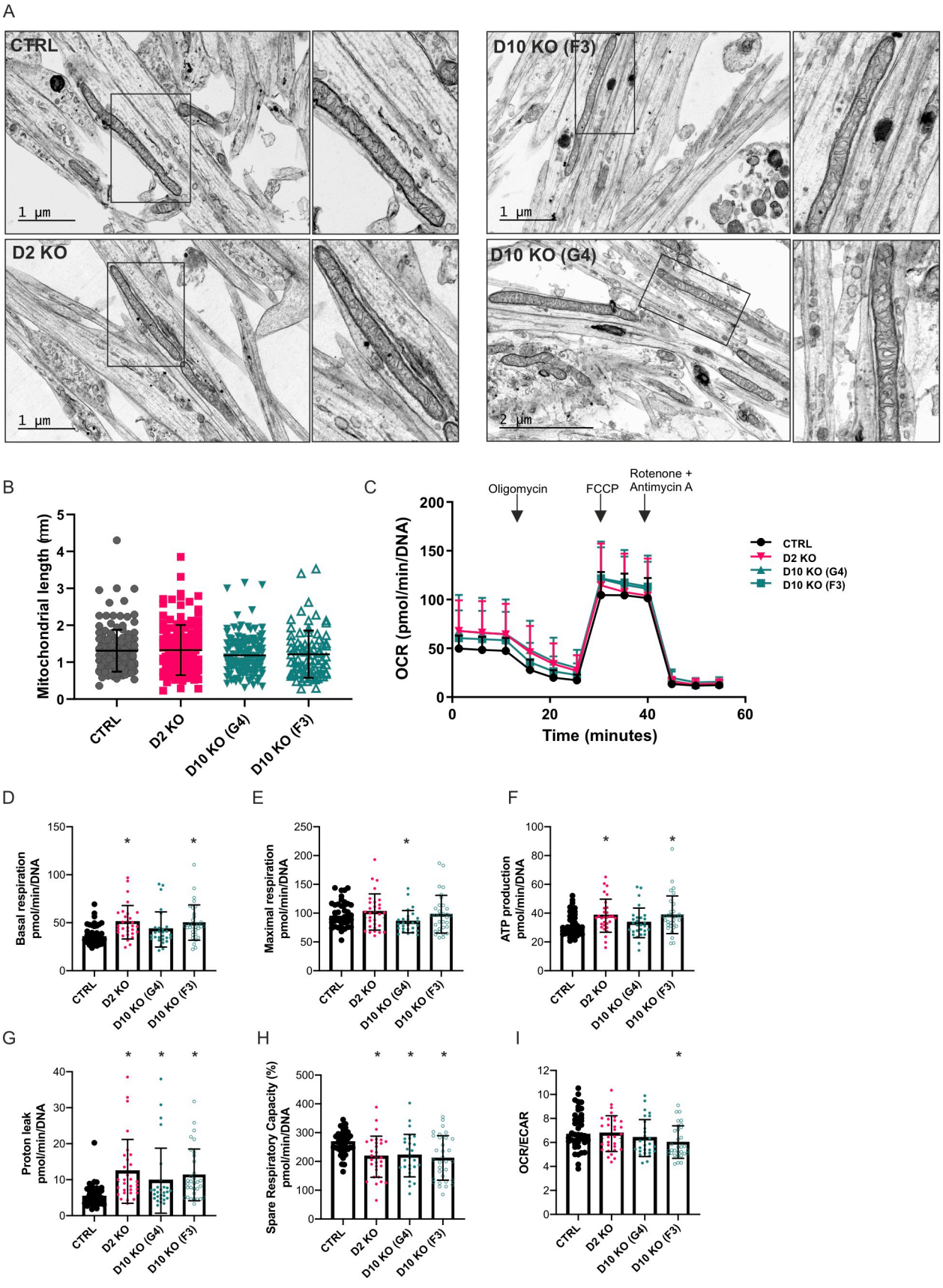

(caption on next page)

Fig. 4. CHCHD2 and CHCHD10 are not dispensable for mitochondrial respiration in human iPSC-derived motor neurons. (A) Ultrastructure analysis by transmission electron microscopy of parental control, D2KO and two D10KO (clones F3 and G4) iPSC-derived motor neurons at day 38. The right panel of each image is a magnification of the area indicated by the square in the left panel. Representative images of motor neuron neurites are shown. Scale bars are indicated. (B) Quantification of mitochondrial length (μm) in electron micrographs (n = 80–143 per clone). (C) OCR in iPSC-derived motor neurons. Arrows indicate when mitochondrial inhibitors were added. (D) Basal respiration. (E) Maximal respiration was assessed following mitochondrial uncoupling by FCCP. (F) ATP-coupled respiration was determined after inhibition of ATP synthase by oligomycin. (G) Proton leakage indicates remaining OCR after inhibiting complex I and III by rotenone and antimycin-A. (H) Spare respiratory capacity (%) is determined by the difference between maximal and basal OCR. (I) Ratio between OCR and extracellular acidification rate (ECAR). Data represent mean ± SD, *P < .05, individual data points are shown from two independent experiments (n = 28–42 replicates/cell line).

acetylcholine is the main neurotransmitter at neuromuscular junction (NMJ), there are indications that glutamate might participate in modulating cholinergic transmission at vertebrate NMJ (Colombo, 2019), where glutamate activates presynaptic ionotropic receptors leading to increased release of acetylcholine to NMJ (Fu et al., 1995; Liou et al., 1996). We also detected altered expression of several K^+-, Na^+- and Ca^{2+}-channel transcripts. Altered excitability has been proposed as one of the underlying causes for ALS (Naujock et al., 2016; Wainger et al., 2014).

We identified highly upregulated expression of *DPP6*, which encodes a single-pass type II membrane protein involved in trafficking of voltage-gated potassium channels (Sun et al., 2011). GWAS associated *DPP6* with susceptibility to sporadic ALS (van Es et al., 2008), and *DPP6* was found as one of the most increased transcripts in iPSC-motor neurons from ALS patients with the *C9ORF72* repeat expansion (Sareen et al., 2013). Another highly upregulated gene in both knockouts was *LYNX1*, which functions as an allosteric modulator of nicotinic acetylcholine receptor, balancing neuronal activity and survival (Miwa et al., 2006). We also saw a reduction of transferrin (*TF*) expression in knockout motor neurons. Transferrin is an extracellular iron transporter, balancing cellular iron uptake with efflux, and it is mainly expressed in liver but also in the nervous system. CHCHD10 knockdown in HEK293 cells was shown to result in accumulation of intramitochondrial iron, leading to a suggestion of CHCHD10 to function as a chaperone in mitochondrial iron import (Burstein et al., 2018). Whether iron levels and transferrin have a role in motor neurons in CHCHD10/2-deficiency remains to be studied.

Taken together, we propose that although functional human motor neuron differentiation in vitro does not require CHCHD2 or CHCHD10, these proteins are not dispensable in motor neuron mitochondria, and their loss results in compensatory responses in respiration and in transcriptional regulation of synaptic function. Whether the insufficient energy metabolism is enough to compromise function for example in a late-onset manner, or in combination with a postsynaptic defect, is not yet known.

Interestingly, a new muscle-specific Chchd10 knockout mouse showed motor defects, abnormal neuromuscular transmission and NMJ structure, suggesting that CHCHD10 has an important role at the peripheral synapse (Xiao et al., 2019). Similarly, the CHCHD10 knockin mice had severe NMJ degeneration and motor behavior defects (Anderson et al., 2019; Genin et al., 2019). Co-cultures of iPSC-derived motor neurons and myotubes could be used to verify whether human NMJ formation is also affected by CHCHD10/2 defects. It is also possible that both the motor neurons and muscle cells contribute to the dying-back motor neuronopathy, as was reported in the case of FUS-ALS, which revealed endplate maturation defects (Picchiarelli et al., 2019). Future studies using more complex culture systems, which better mimic the physiological environment and interactions of motor neurons, are required to address the consequences that the identified synaptic alterations may have in deficiency of CHCHD2 and CHCHD10. Furthermore, iPSC-based models of the human disease variants that cause motor neuron disease phenotypes or Parkinson's disease should be compared to the knockout models to gain further understanding of the genetic mechanisms of the diseases.

In conclusion, we have presented functional differentiation of human iPSC-derived motor neurons in the absence of CHCHD10 or CHCHD2, with compensatory effects. Similar effects on respiration and transcriptome profiles in both knockouts support a similar role for the two proteins in the mitochondria of motor neurons.

4. Experimental procedures

4.1. Ethical approval

The generation of the human induced pluripotent stem cell lines used in this study was approved by the Coordinating Ethics Committee of the Helsinki and Uusimaa Hospital District (Nro 423/13/03/00/08) with informed consent of the donor.

4.2. Induced pluripotent stem cells (iPSC)

The reprogramming of human neonatal foreskin fibroblasts from healthy control (HEL46.11) into pluripotent stem cells by Sendai virus technology has been done at Biomedicum Stem Cell Center (University of Helsinki, Finland), as previously described (Trokovic et al., 2015), and the pluripotency confirmed in previous studies (Saarimäki-Vire et al., 2017; Weltner et al., 2018). Cells were cultured at 37 °C in 5% CO2, 20% O2. Using the HEL46.11 iPSC line as the parental control, we generated one D2KO clone and four D10KO clones (F3, F2, G4 and B9), of which we used F3, F2 and G4 in most of the studies. IPSC were maintained on Matrigel-coated (Corning) plates with E8-medium (Gibco) supplemented with E8-supplement (Gibco). IPSC were passaged with 0.5 mM EDTA (Invitrogen) in phosphate-buffer saline (PBS) when confluent. Pluripotency of the generated knockout iPSC lines was confirmed with immunostaining with Nanog (1:250 dilution, D73G4, Cell Signaling) and TRA-1-81 (1:100, MA1-024, ThermoFisher) antibodies. In addition, expression levels of *OCT4* and *SOX2* were analyzed by qRT-PCR.

4.3. Genome editing of iPSC

CRISPR-*Sp*Cas9 technology was used to generate D2KO and D10KO iPSC. GuideRNA (gRNAs) sequences were designed using web-based tools from http://crispr.mit.edu (Hsu et al., 2013) and https://benchling.com (Benchling [Biology Software], 2018). The gRNAs were designed to target 5′UTR and the first exon. Transcriptional units for gRNA expression were prepared by PCR amplification and further concatenated using Golden Gate assembly as described in (Balboa et al., 2015), detailed protocol is provided by Addgene (http://www.addgene.org/78311/). Different gRNA pairs were first tested by co-transfection with wild type spCas9 expressing the plasmid CAG-Cas9-T2A-EGFP-ires-puro (Addgene plasmid #78311) into HEK293 cells. The genomic region flanking gRNA target sites was amplified with a pair of gene specific primers and editing efficiency was detected by agarose gel electrophoresis.

Sequences (5′-TGGAAGAGCAGGACGTCACG-3′) and (5′-GTGCGGC TTCGGCTTCCACG-3′) in the 5′UTR and first exon, respectively, were chosen for the CRISPR-SpCas9 targeting sites in *CHCHD2*. Similarly, gRNAs used to create *CHCHD10* knockout were (5′-TCTGTTAGGACC ACCGCAGA-3′) and (5′-GCCGCGCTGCGGCTTCCCCG-3′). Genome editing was done essentially as described in (Saarimäki-Vire et al., 2017). Briefly, two million HEL46.11 cells were electroporated with

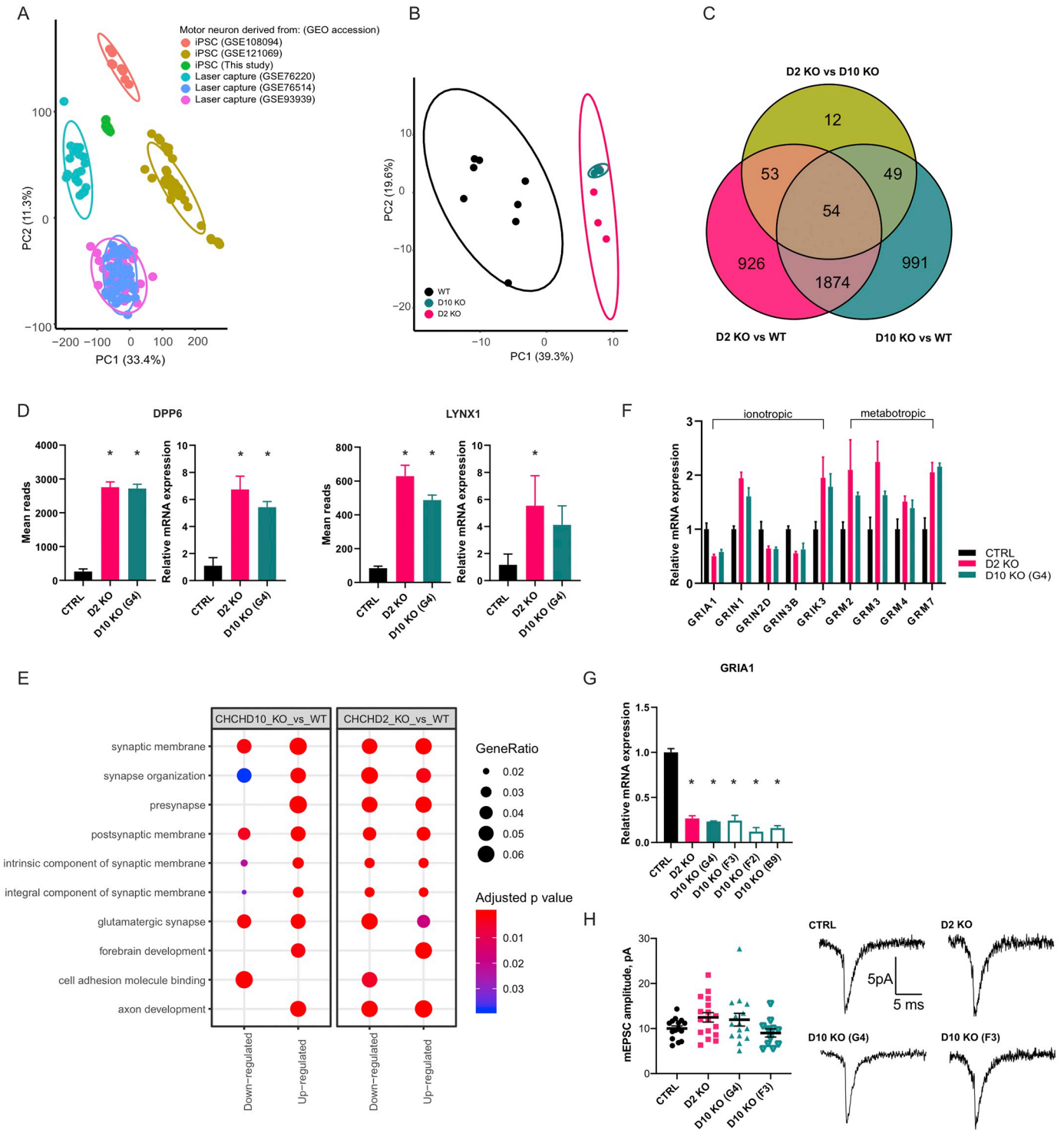

Fig. 5. CHCHD2 and CHCHD10 knockout motor neuron transcriptome profiles are overlapping and show altered synaptic gene expression. (A) Comparison of our RNA sequencing dataset by principal component analysis (PCA) to available human iPSC-motor neuron and laser captured post mortem human motor neurons. (B) PCA of motor neurons of this study show overlap for D2KO and D10KO motor neurons (n = 8 for parental control (WT) and n = 4 for each KO). (C) Venn diagram displaying the number of significantly altered genes (FDR < 0.01) in D10KO vs. WT, D2KO vs. D10KO and D2KO vs. WT samples. (D) Mean reads of *DPP6* and *LYNX1* in RNA sequencing dataset (left panels), and expression of the same genes by qRT-PCR (right panels) from independent samples (n = 3 per clone). (E) GO term enriched pathways in D10KO vs. WT and D2KO vs. WT comparisons. Up- and downregulated pathways are indicated by gene ratio and FDR. (F) Significantly altered (FDR < 0.01) glutamate receptor subunits. Mean reads from RNA sequencing were normalized to parental control level, shown as relative expression. (G) qRT-PCR of *GRIA1* normalized to *GAPDH*. Individual D10 KO clones shown (n = 3 independent experiments). (H) Amplitudes (pA) of miniature excitatory post-synaptic currents (mEPSCs) (n = 11–17 per clone) and representative traces of mEPSCs. Data are shown as mean ± SD, * P < .05.

Table 2
Kinetics of the AMPA receptor-mediated EPSCs.

	Parental control (n)	D2KO (n)	D10KO F3 (n)	D10KO G4 (n)
Rise time, ms	2.08 ± 0.25 (15)	2.80 ± 0.45 (17)	1.39 ± 0.16 (11)	2.00 ± 0.33 (15)
Decay time, ms	2.67 ± 0.35 (15)	3.55 ± 0.58 (17)	1.61 ± 0.15 (11)	2.45 ± 0.36 (15)
Peak half-width, ms	1.28 ± 0.15 (15)	1.58 ± 0.23 (17)	0.77 ± 0.07 (11)	1.21 ± 0.18 (15)

n = number of cells tested. *p < .05 compared to parental control.

3 μg of CAG-Cas9-T2A-EGFP-ires-puro endotoxin-free plasmid and 500 ng of each gRNA (Neon Transfection System, 1100 V, 20 ms, two pulses, Thermo Fisher Scientific). Electroporated cells were immediately plated onto prewarmed Matrigel-coated plates containing E8-medium with 10 μM ROCK inhibitor (ROCKi) (Y-27632 2HCl, Selleckchem). Alive, singlet cells positive for GFP fluorescence were sorted on 96-well Matrigel-coated plates containing E8 medium supplemented with 5 μM ROCKi and CloneR™ (StemCell Technologies) using BDInflux Flow Cytometer at the Biomedicum Flow Cytometry Unit (University of Helsinki, Finland). Expandable iPSC colonies were screened by PCR followed by sequencing and subsequently by western blotting.

4.4. Motor neuron differentiation

To differentiate iPSCs into motor neurons, we used the protocol by (Guo et al., 2017; Maury et al., 2015) with slight modifications. Briefly, to obtain neuroepithelial stem cells, iPSC were dissociated with Accutase (Gibco) into small clusters and resuspended in E8 medium containing 5 μM Y-27632 (Selleckchem). The following day, medium was changed to Neuronal basal medium (DMEM F12, Neurobasal vol:vol, with N2 (Life Technologies), B27 (Life technologies) and L-ascorbic acid 0.1 mM (Santa Cruz)) supplemented with 40 μM SB431542 (Merck), 0.2 μM LDN-193189 (Merck/Sigma), 3 μM CHIR99021 (Selleckchem), and 5 μM Y-27632 (Selleckchem). From day 3 on, 0.1 μM retinoic acid (Fisher) and 0.5 μM SAG (Calbiochem) was added to neurobasal medium. From day 7 on, BDNF (10 ng/ml, Peprotech) and GDNF (10 ng/ml, Peprotech) were added. 20 μM DAPT (Calbiochem) was added on day 9. Motor neuron progenitor spheroids were dissociated into single cells for plating on day 11 by using Accumax (Invitrogen). Motor neuron progenitors were subsequently plated on poly-D-lysine 50 μg/ml (Merck Millipore) and laminin 10 μg/ml (Sigma-Aldrich) coated plates at 5×10^4 cells per cm^2. At day 14 retinoic acid and SAG were removed from media. From day 16 on, the cells were switched to motor neuron maturation medium supplemented with BDNF, GDNF, and CNTF (each 10 ng/ml, Peprotech). Media were changed every other day by replacing half of the medium. Motor neurons were ISL1-positive around day 30 of differentiation, after which they were considered mature. Motor neurons were used in experiments at week 5, except at week 7 in patch clamp.

4.5. Immunoblotting

For protein analysis iPSC and iPSC-derived motor neurons were manually collected by scraping on ice and samples were maintained at −80 °C until further processing. For western blot, total protein from motor neuronal and iPSC cultures were harvested with RIPA buffer (Thermo Fisher) supplemented with Halt™ protease inhibitor (Thermo Scientific). Protein concentration was quantified with BCA assay (Pierce) according to manufacturer's instructions. 10 μg of protein/sample was run on TGX 10% and 4–20% acrylamide gels (Bio-Rad) and transferred to 0.2 μm PVDF-membrane (Bio-Rad) with the TransBlot Turbo transfer system (Bio-Rad). Membrane was blocked with 5% milk/TBS-T for 1 h RT. The primary and secondary antibodies are listed in supplementary materials. Signal was detected with ECL reagent (Thermo Scientific) and membranes were imaged with Chemidoc XRS + (Bio-Rad). Image Lab Software (BioRad) was used to quantify the band intensities. For quantification, band intensities were normalized to GAPDH or HSP60.

Assembly of mitochondrial respiratory chain complexes were investigated using Blue-Native-PAGE in mitochondria extracted from iPSC as described by (Konovalova, 2019), using primary and secondary antibodies listed in supplementary materials.

4.6. Quantitative PCR (qPCR) based determination of mitochondrial DNA copy number

DNA was extracted with Macherey-Nagel™ NucleoSpin™. 25 ng of DNA was used for the qPCR reaction. Levels of mitochondrial tRNA-LEU (UUR) (*MT-TL1*) and nuclear *B2M* were analyzed by qPCR amplification in CFX Real-time system C1000Touch (Bio-Rad) with SYBR-green Flash (Thermo Fisher) by transcript specific primers. The ratio between *MT-TL1* and *B2M* transcripts were used to determine the copy number of mtDNA. The ratio between mitochondrial cytochrome B (*MT-CYTB*) or nuclear *ACTB* transcripts were used to verify results.

4.7. Immunocytochemistry

IPSC and iPSC-derived motor neuronal cultures on cover glasses were fixed with 4% paraformaldehyde (PFA) for 15 min at RT and then permeabilized with PBS containing 0.2% Triton X-100 (Fisher) for 10 min. Cells were blocked with 5% protease-free BSA (Jackson Immuno Research) in 0.1% Tween20 in PBS (PBS-T) for 2 h in RT. Cells were incubated overnight at +4 °C in blocking buffer (5% bovine serum) containing different primary antibodies, listed in supplementary materials. After washing with PBS-T, cells were incubated with secondary antibody for 1 h at RT. Cover glasses were applied on microscope slides with Vectashield DAPI (#H-1200) and imaged with Axio Observer Z1 (Zeiss) inverted fluorescence microscope.

IPSCs with CHCHD2/10 (Alexa 488) staining were imaged with LSM880 IndiMo Axio Observed laser scanning confocal microscope with Plan-Apochromat 63×/1.4 oil DIC M27 immersion lense. CHCHD2/10 channel was captured with 488 laser using the same settings and exposure time for all samples (laser 3.06%). Images were acquired at 16-bit depth and 1912-x1912 frame size. The results were visualized with Zen Blue software.

4.8. Quantitative reverse transcription PCR (qRT-PCR)

RNA from differentiated motor neuronal cultures was isolated using NucleoSpin RNA extraction kit (Macherey-Nagel). RNA was reverse transcribed with Maxima first strand cDNA synthesis kit (Thermo Fisher). cDNA levels were analyzed by qRT-PCR amplification in CFX Real-time system C1000T (Bio-Rad) with SYBR green Flash (Thermo Fisher) by transcript specific primers. Technical duplicates were used for all studies. 2 ng of cDNA was used for total mRNA quantification. Relative quantification was done using the ΔΔCt method with normalization to *GAPDH*. A list of primers can be found at supplementary methods.

4.9. Transmission electron microscopy (TEM)

Motor neuronal cultures on glass slides/cover glasses were fixed

with 2% glutaraldehyde in 0.1 M NaCac buffer for 30 min at RT, and then washed with NaCac buffer. Cells were kept in NaCac buffer at +4 °C until further use. iPSC on glass slides were fixed with 2% PFA + 2% Glutaraldehyde (Sigma) for 30 min at 4 °C, then washed once with PBS and fixed with 2% Glutaraldehyde O/N at 4 °C. Fixed neurons and iPSC were prepared according to standard protocols for transmission electron microscopy. Ultrathin sections were observed with Jeol 1400 transmission electron microscope at 80000 V. ImageJ (https://imagej.nih.gov/ij/) package Fiji (Schindelin et al., 2012) was used to assess mitochondria length.

4.10. ATP assay

Intracellular ATP levels of iPSCs were quantified using an ATPlite assay kit (PerkinElmer). IPSCs were dissociated with Accutase (Gibco) and cell suspension containing 15,000 cells was added to 96-well microplate. IPSCs were processed according to manufacturer's instructions. Briefly, cells were lysed with mammalian lysis solution at orbital shaker 700 rpm for 5 min. After lysis, ATP substrate was added and mixed at orbital shaker 700 rpm for 5 min. Plate was allowed to dark adapt for 10 min, after which luminescence intensities were monitored with EnSpire (PerkinElmer) microplate reader with 0.1 s measurement time. Total ATP amount was quantified from ATP standard curve.

4.11. Oxygen consumption

Oxygen consumption rate in iPSC and iPSC-derived motor neurons was measured using Seahorse XF96 Extracellular Flux Analyzer (Agilent) as previously described in (Vandoorne et al., 2019). Briefly, IPSC were seeded at density of 25,000 cells/well 24 h prior measurements on Matrigel-coated (Corning) XF96 Seahorse plates in the presence of 10 μM Y-27632 (Selleckchem) (Zhang et al., 2012). iPSC oxygen consumption rate (OCR) was measured one day after seeding. At day 10 of differentiation iPSC-derived motor neuron progenitors were seeded at density of 20,000 cells/well on poly-D-lysine and laminin coated XF96 Seahorse plates (Agilent). Oxygen consumption rate (OCR) was measured at day 30 of motor neuron differentiation. On the day of the assay, medium was replaced with Seahorse Base Medium supplemented with 1 mM pyruvate, 2 mM glutamine, 25 mM glucose and 5 mM HEPES, pH adjusted to 7.4. In baseline conditions, three measurements of OCR were done, after which ATP synthetase was inhibited by injection of oligomycin (Sigma) (concentration in well 1.5 μM for iPSC and 2 μM for iPSC-derived motor neurons). Oligomycin induced drop in baseline OCR reflects oxygen consumption needed for ATP production. Next, uncoupler carbonilcyanide *p*-triflouromethoxyphenylhydrazone (FCCP) (Sigma) was injected (concentration in well 0.25 μM for iPSC and 5 μM for iPSC derived motor neurons). FCCP injection forces cells to use their maximal mitochondrial capacity to maintain membrane potential and increase in OCR reflects the spare respiratory capacity. Finally, electron transport chain was shut down by inhibiting complex I and III activity by addition of rotenone (Sigma) and antimycin-A (Sigma) at 1 μM concentration in well and remaining OCR reflects non-mitochondrial oxygen consumption. Difference in OCR between oligomycin and rotenone/antimycin-A injection indicates proton leakage. After assay, iPSC were stained with Hoechst and OCR was normalized to cell number using Cytation5 plate reader. iPSC-derived motor neurons were normalized to DNA content using CyQUANT kit (Invitrogen). Three independent runs (two for motor neurons) were performed, where each run contained 23 wells per cell line. Only those wells with a homogeneous monolayer of iPSC or intact neuronal culture were included in the analysis.

4.12. RNA sequencing

RNA was isolated from four independent motor neuron cultures per knockout cell line (D2KO and D10KO G4 and F3) and from eight control cultures at day 37 of differentiation. RNA was extracted with Nucleospin RNA kit (Macherey-Nagel) according to manufacturer's instructions including rDNAse treatment. RNA concentration was measured with Qubit. RNA quality determination and mRNA sequencing were done at Biomedicum Functional Genomics Unit with single-end sequencing with poly(A) binding beads and NEBNext Ultra Directional RNA Library Prep and sequenced with Illumina NextSeq High Output 1 × 75 bp.

Raw data was demultiplexed with bcl2fastq2 (v2.20.0.422; Illumina). Adapter sequences (AGATCGGAAGAGCACACGTCTGAACTC CAGTCA), low quality (Phred score < 25) and ambiquous bases (N) were removed with cutadapt (v.2.2) (Martin, 2011), retaining reads longer than 25 bp. The trimmed reads were mapped to the human reference genome (GRCh38) with STAR (v. 2.5.3) (Dobin et al., 2013). Gene expression was analyzed with R (v.3.6.0) (R Core Team, 2019). The read counts for genes (mapping to exons) were extracted with Rsubreads (v.1.34.6) (Liao et al., 2019) excluding duplicates, multimapping reads, chimeric fragments, and reads with mapping quality below 10.

Differential gene expression was analyzed with DESeq2 (v.1.24) (Love et al., 2014), comparing D2KO and D10KO to parental cells. The differentially expressed genes were analyzed for pathway enrichment using the GO (Ashburner et al., 2000; The Gene Ontology Consortium, 2018), using ClusterProfiler (v3.12.0) (Yu et al., 2012). For enrichment analysis, the set of background genes (universe) was limited to genes expressed in our samples. Genes with low read depth (< 50 reads in total) were excluded from the differential expression and enrichment analysis.

RNA-seq data from the motor neurons in this study were contrasted to publicly available datasets of other human iPSC derived motor neurons; GSE108094 (Rizzo et al., 2019) and GSE121069 (Nijssen et al., 2018) as well as laser captured motor neurons; GSE76220 (Batra et al., 2016), GSE76514 (Nichterwitz et al., 2016) and GSE93939 (Allodi et al., 2019). The same analysis procedures (trimming, mapping and read counting) were applied to the reference samples as for our dataset. Gene expression results were visualized with ggplot2 (v3.2.1) (Wickham, 2016), limma (v3.40.6) (Ritchie et al., 2015) and eulerr (v5.1.0) (Larsson, 2019).

4.13. Electrophysiology

Whole-cell patch-clamp recordings were done on living cells after 42 days in culture. Coverslips containing cultured neurons were placed to recording chamber on the visually guided patch-clamp setup. Temperature at the recording chamber was kept at 30 °C, and cells were continuously perfused with ACSF of the following composition (mM): 124 mM NaCl, 3 mM KCl, 1.25 mM NaH_2PO_4, 1 mM $MgSO_4$, 26 mM $NaHCO_3$, 2 mM $CaCl_2$, 15 mM glucose, and 95% O_2/5% CO_2. Recordings were done with glass microelectrodes (4–6 MΩ), using Multiclamp 700A amplifier (Axon Instruments, USA), and digitized at 20 kHz. Data were collected with Clampex 10.2 (Molecular Devices, USA). Series resistance, input resistance and capacitance were recorded in voltage clamp mode at −70 mV by injection of 5 mV voltage steps. If series resistance exceeded 20 MΩ, or if the change in series resistance during the experiment exceeded 30%, the recording was discarded.

For recording of passive membrane properties, voltage-gated currents and action potential firing microelectrodes were filled with the intracellular solution containing (mM): 105 K gluconate, 15 KCl, 5.3 $CaCl_2$, 5 NaCl, 10 HEPES, 10 EGTA, 4 MgATP, 0.5 Na_2GTP, pH 7.2. Voltage-gated sodium/calcium and potassium currents were recorded in voltage clamp mode. Baseline voltage was set at −70 mV, and voltage steps with the increasing increment of 10 mV were injected for 100 ms. Leak subtraction protocol was applied, and the current amplitude was analyzed after correction for leak current. Resting membrane potential and spontaneous activity were recorded in current clamp mode without any background current injected. For recording of the evoked action potentials, baseline membrane potential was held at

−60 mV, and depolarizing current steps with the increasing increment of 10 pA were injected for 1 s.

Miniature excitatory synaptic currents (mEPSCs) were recorded in a whole-cell voltage clamp configuration at −70 mV in ACSF containing tetrodotoxin (TTX, 1 μM) and picrotoxin (100 μM). Presence of AMPA-type glutamatergic synapses was confirmed by disappearance of spontaneous EPSCs by addition of NBQX (20 μM). Intracellular solution contained (in mM): 110 $CsMeSO_3$, 5.3 $CaCl_2$, 5 NaCl, 10 HEPES, 10 EGTA, 5 lidocaine N-ethyl chloride, 4 MgATP, 0.5 Na_2ATP.

Data were analyzed in Clampfit 10.2 (Molecular Devices, USA) and MiniAnalysis program (Synaptosoft). Properties of individual evoked action potentials were analyzed by a custom MATLAB script (MATLAB R2018b, MathWorks, USA; Zubarev, Nagaeva, unpublished). Meta-analysis was done in GraphPad Prism 8.

4.14. Statistical analysis

GraphPad Prism was used for all statistical analyses except RNA-seq. Unless otherwise indicated, mean ± SD values are reported in the graphs. One-way ANOVA was used for the experiments with post-hoc Tukey's test to determine statistical differences between groups. Student's unpaired two-tailed *t*-test was used to determine statistical significance in OCR measurements. *P < .05 were considered significant.

Supplementary data to this article can be found online at https://doi.org/10.1016/j.nbd.2020.104940.

Data availability

Differential expression analysis and raw data for the RNA-Seq are deposited at NCBI Gene Expression Omnibus under the accessions GSE133764 (CHCHD2 KO) and GSE133763 (CHCHD10 KO).

Declaration of Competing Interest

The authors declare no competing interests.

Acknowledgments

We thank Riitta Lehtinen for technical assistance. We acknowledge Biomedicum Stem Cell Centre, Biomedicum Functional Genomics Unit, Biomedicum Imaging Unit, and Electron Microscopy Unit of the Institute of Biotechnology, University of Helsinki. HiLIFE Flow cytometry unit is acknowledged for assistance with cell sorting. This work was supported by the Academy of Finland (MetaStem Centre of Excellence to H.T., Clinical Researcher Funding to E.Y.), Sigrid Juselius Foundation, University of Helsinki, Emil Aaltonen Foundation, and Helsinki University Hospital.

References

Allodi, I., Nijssen, J., Benitez, J.A., Schweingruber, C., Fuchs, A., Bonvicini, G., Cao, M., Kiehn, O., Hedlund, E., 2019. Modeling motor neuron resilience in ALS using stem cells. Stem Cell Rep. 12, 1329–1341. https://doi.org/10.1016/j.stemcr.2019.04.009.

Anderson, C.J., Bredvik, K., Burstein, S.R., Davis, C., Meadows, S.M., Dash, J., Case, L., Milner, T.A., Kawamata, H., Zuberi, A., Piersigilli, A., Lutz, C., Manfredi, G., 2019. ALS/FTD mutant CHCHD10 mice reveal a tissue-specific toxic gain-of-function and mitochondrial stress response. Acta Neuropathol. https://doi.org/10.1007/s00401-019-01989-y.

Aras, S., Bai, M., Lee, I., Springett, R., Hüttemann, M., Grossman, L.I., 2015. MNRR1 (formerly CHCHD2) is a bi-organellar regulator of mitochondrial metabolism. Mitochondrion 20, 43–51. https://doi.org/10.1016/J.MITO.2014.10.003.

Ashburner, M., Ball, C.A., Blake, J.A., Botstein, D., Butler, H., Cherry, J.M., Davis, A.P., Dolinski, K., Dwight, S.S., Eppig, J.T., Harris, M.A., Hill, D.P., Issel-Tarver, L., Kasarskis, A., Lewis, S., Matese, J.C., Richardson, J.E., Ringwald, M., Rubin, G.M., Sherlock, G., 2000. Gene ontology: tool for the unification of biology. Nat. Genet. 25, 25–29. https://doi.org/10.1038/75556.

Auranen, M., Ylikallio, E., Shcherbii, M., Paetau, A., Kiuru-Enari, S., Toppila, J.P., Tyynismaa, H., 2015. CHCHD10 variant p.(Gly66Val) causes axonal Charcot-Marie-Tooth disease. Neurol. Genet. 1, e1. https://doi.org/10.1212/NXG.0000000000000003.

Balboa, D., Weltner, J., Eurola, S., Trokovic, R., Wartiovaara, K., Otonkoski, T., 2015. Conditionally stabilized dCas9 activator for controlling gene expression in human cell reprogramming and differentiation. Stem Cell Rep. 5, 448–459. https://doi.org/10.1016/j.stemcr.2015.08.001.

Bannwarth, S., Ait-El-Mkadem, S., Chaussenot, A., Genin, E.C., Lacas-Gervais, S., Fragaki, K., Berg-Alonso, L., Kageyama, Y., Serre, V., Moore, D.G., Verschueren, A., Rouzier, C., Le Ber, I., Augé, G., Cochaud, C., Lespinasse, F., N'guyen, K., De Septenville, A., Brice, A., Yu-Wai-Man, P., Sesaki, H., Pouget, J., Paquis-Flucklinger, V., 2014. A mitochondrial origin for frontotemporal dementia and amyotrophic lateral sclerosis through CHCHD10 involvement. Brain 137, 2329–2345. https://doi.org/10.1093/brain/awu138.

Batra, R., Hutt, K., Vu, A., Rabin, S.J., Baughn, M.W., Libby, R.T., Hoon, S., Ravits, J., Yeo, G.W., 2016. Gene expression signatures of sporadic ALS motor neuron populations. bioRxiv 38448. https://doi.org/10.1101/038448.

Becker, T., Böttinger, L., Pfanner, N., 2012. Mitochondrial protein import: from transport pathways to an integrated network. Trends Biochem. Sci. 37, 85–91. https://doi.org/10.1016/j.tibs.2011.11.004.

Brockmann, S.J., Freischmidt, A., Oeckl, P., Müller, K., Ponna, S.K., Helferich, A.M., Paone, C., Reinders, J., Kojer, K., Orth, M., Jokela, M., Auranen, M., Udd, B., Hermann, A., Danzer, K.M., Lichtner, P., Walther, P., Ludolph, A.C., Andersen, P.M., Otto, M., Kursula, P., Just, S., Weishaupt, J.H., 2018. CHCHD10 mutations p. R15L and p. G66V cause motoneuron disease by haploinsufficiency. Hum. Mol. Genet. 27, 706–715. https://doi.org/10.1093/hmg/ddx436.

Burstein, S.R., Valsecchi, F., Kawamata, H., Bourens, M., Zeng, R., Zuberi, A., Milner, T.A., Cloonan, S.M., Lutz, C., Barrientos, A., Manfredi, G., 2018. In vitro and in vivo studies of the ALS-FTLD protein CHCHD10 reveal novel mitochondrial topology and protein interactions. Hum. Mol. Genet. 27, 160–177. https://doi.org/10.1093/hmg/ddx397.

Cavallaro, G., 2010. Genome-wide analysis of eukaryotic twin CX9C proteins. Mol. BioSyst. 6, 2459–2470. https://doi.org/10.1039/c0mb00058b.

Colombo, Francolini, 2019. Glutamate at the vertebrate neuromuscular junction: from modulation to neurotransmission. Cells 8, 996. https://doi.org/10.3390/cells8090996.

Dobin, A., Davis, C.A., Schlesinger, F., Drenkow, J., Zaleski, C., Jha, S., Batut, P., Chaisson, M., Gingeras, T.R., 2013. STAR: ultrafast universal RNA-seq aligner. Bioinformatics 29, 15–21.

van Es, M.A., van Vught, P.W., Blauw, H.M., Franke, L., Saris, C.G., Van Den Bosch, L., de Jong, S.W., de Jong, V., Baas, F., van't Slot, R., Lemmens, R., Schelhaas, H.J., Birve, A., Sleegers, K., Van Broeckhoven, C., Schymick, J.C., Traynor, B.J., Wokke, J.H., Wijmenga, C., Robberecht, W., Andersen, P.M., Veldink, J.H., Ophoff, R.A., van den Berg, L.H., 2008. Genetic variation in DPP6 is associated with susceptibility to amyotrophic lateral sclerosis. Nat. Genet. 40, 29–31. https://doi.org/10.1038/ng.2007.52.

Fu, W.M., Liou, J.C., Lee, Y.H., Liou, H.C., 1995. Potentiation of neurotransmitter release by activation of presynaptic glutamate receptors at developing neuromuscular synapses of Xenopus. J. Physiol. 489, 813–823. https://doi.org/10.1113/jphysiol.1995.sp021094.

Funayama, M., Ohe, K., Amo, T., Furuya, N., Yamaguchi, J., Saiki, S., Li, Y., Ogaki, K., Ando, M., Yoshino, H., Tomiyama, H., Nishioka, K., Hasegawa, K., Saiki, H., Satake, W., Mogushi, K., Sasaki, R., Kokubo, Y., Kuzuhara, S., Toda, T., Mizuno, Y., Uchiyama, Y., Ohno, K., Hattori, N., 2015. CHCHD2 mutations in autosomal dominant late-onset Parkinson's disease: a genome-wide linkage and sequencing study. Lancet Neurol. 14, 274–282. https://doi.org/10.1016/S1474-4422(14)70266-2.

Genin, E.C., Plutino, M., Bannwarth, S., Villa, E., Cisneros-Barroso, E., Roy, M., Ortega-Vila, B., Fragaki, K., Lespinasse, F., Pinero-Martos, E., Auge, G., Moore, D., Burte, F., Lacas-Gervais, S., Kageyama, Y., Itoh, K., Yu-Wai-Man, P., Sesaki, H., Ricci, J.-E., Vives-Bauza, C., Paquis-Flucklinger, V., 2016. CHCHD10 mutations promote loss of mitochondrial cristae junctions with impaired mitochondrial genome maintenance and inhibition of apoptosis. EMBO Mol. Med. 8, 58–72. https://doi.org/10.15252/emmm.201505496.

Genin, E.C., Madji Hounoum, B., Bannwarth, S., Fragaki, K., Lacas-Gervais, S., Mauri-Crouzet, A., Lespinasse, F., Neveu, J., Ropert, B., Augé, G., Cochaud, C., Lefebvre-Omar, C., Bigou, S., Chiot, A., Mochel, F., Boillée, S., Lobsiger, C.S., Bohl, D., Ricci, J.E., Paquis-Flucklinger, V., 2019. Mitochondrial defect in muscle precedes neuromuscular junction degeneration and motor neuron death in CHCHD10 S59L/+ mouse. Acta Neuropathol. https://doi.org/10.1007/s00401-019-01988-z.

Guo, W., Naujock, M., Fumagalli, L., Vandoorne, T., Baatsen, P., Boon, R., Ordovás, L., Patel, A., Welters, M., Vanwelden, T., Geens, N., Tricot, T., Benoy, V., Steyaert, J., Lefebvre-Omar, C., Boesmans, W., Jarpe, M., Sterneckert, J., Wegner, F., Petri, S., Bohl, D., Vanden Berghe, P., Robberecht, W., Van Damme, P., Verfaillie, C., Van Den Bosch, L., 2017. HDAC6 inhibition reverses axonal transport defects in motor neurons derived from FUS-ALS patients. Nat. Commun. 8, 861. https://doi.org/10.1038/s41467-017-00911-y.

Hsu, P.D., Scott, D.A., Weinstein, J.A., Ran, F.A., Konermann, S., Agarwala, V., Li, Y., Fine, E.J., Wu, X., Shalem, O., Cradick, T.J., Marraffini, L.A., Bao, G., Zhang, F., 2013. DNA targeting specificity of RNA-guided Cas9 nucleases. Nat. Biotechnol. 31, 827–832. https://doi.org/10.1038/nbt.2647.

Huang, X., Wu, B.P., Nguyen, D., Liu, Y.-T., Marani, M., Hench, J., Bénit, P., Kozjak-Pavlovic, V., Rustin, P., Frank, S., Narendra, D.P., 2018. CHCHD2 accumulates in distressed mitochondria and facilitates oligomerization of CHCHD10. Hum. Mol. Genet. https://doi.org/10.1093/hmg/ddy340.

Konovalova, S., 2019. Analysis of mitochondrial respiratory chain complexes in cultured human cells using blue native polyacrylamide gel electrophoresis and immunoblotting. J. Vis. Exp., e59269. https://doi.org/10.3791/59269.

Larsson, J., 2019. Eulerr: Area-Proportional Euler and Venn Diagrams with Ellipses. R

Packag. Version.
Liao, Y., Smyth, G.K., Shi, W., 2019. The R package Rsubread is easier, faster, cheaper and better for alignment and quantification of RNA sequencing reads. Nucleic Acids Res. 47, e47. https://doi.org/10.1093/nar/gkz114.
Liou, H.-C., Yang, R.-S., Fu, W.-M., 1996. Potentiation of spontaneous acetylcholine release from motor nerve terminals by glutamate in *Xenopus tadpoles*. Neuroscience 75, 325–331. https://doi.org/10.1016/0306-4522(96)00280-1.
Liu, Yi-Ting, Huang, Xiaoping, Nguyen, Diana, Sekine, Shammas, Beverly, Wu, Danielle A, Dombi, Eszter, Springer, Joanna, Poulton, Shiori, Sekine, Narendra, Derek P, 2019. Loss of CHCHD2 and CHCHD10 activates OMA1 peptidase to disrupt mitochondrial cristae phenocopying patient mutations. Human Mol. Genet. https://doi.org/10.1093/hmg/ddaa077. ddaa077.
Longen, S., Bien, M., Bihlmaier, K., Kloeppel, C., Kauff, F., Hammermeister, M., Westermann, B., Herrmann, J.M., Riemer, J., 2009. Systematic analysis of the twin cx(9)c protein family. J. Mol. Biol. 393, 356–368. https://doi.org/10.1016/j.jmb.2009.08.041.
Love, M.I., Huber, W., Anders, S., 2014. Moderated estimation of fold change and dispersion for RNA-seq data with DESeq2. Genome Biol. 15, 550. https://doi.org/10.1186/s13059-014-0550-8.
Martin, M., 2011. Cutadapt removes adapter sequences from high-throughput sequencing reads. EMBnet. J. 17, 10.
Maury, Y., Côme, J., Piskorowski, R.A., Salah-Mohellibi, N., Chevaleyre, V., Peschanski, M., Martinat, C., Nedelec, S., 2015. Combinatorial analysis of developmental cues efficiently converts human pluripotent stem cells into multiple neuronal subtypes. Nat. Biotechnol. 33, 89–96. https://doi.org/10.1038/nbt.3049.
Meng, H., Yamashita, C., Shiba-Fukushima, K., Inoshita, T., Funayama, M., Sato, S., Hatta, T., Natsume, T., Umitsu, M., Takagi, J., Imai, Y., Hattori, N., 2017. Loss of Parkinson's disease-associated protein CHCHD2 affects mitochondrial crista structure and destabilizes cytochrome c. Nat. Commun. 8. https://doi.org/10.1038/ncomms15500.
Miwa, J.M., Stevens, T.R., King, S.L., Caldarone, B.J., Ibanez-Tallon, I., Xiao, C., Fitzsimonds, R.M., Pavlides, C., Lester, H.A., Picciotto, M.R., Heintz, N., 2006. The prototoxin lynx1 acts on nicotinic acetylcholine receptors to balance neuronal activity and survival in vivo. Neuron 51, 587–600. https://doi.org/10.1016/j.neuron.2006.07.025.
Müller, K., Andersen, P.M., Hübers, A., Marroquin, N., Volk, A.E., Danzer, K.M., Meitinger, T., Ludolph, A.C., Strom, T.M., Weishaupt, J.H., 2014. Two novel mutations in conserved codons indicate that CHCHD10 is a gene associated with motor neuron disease. Brain. https://doi.org/10.1093/brain/awu227.
Naujock, M., Stanslowsky, N., Bufler, S., Naumann, M., Reinhardt, P., Sterneckert, J., Kefalakes, E., Kassebaum, C., Bursch, F., Lojewski, X., Storch, A., Frickenhaus, M., Boeckers, T.M., Putz, S., Demestre, M., Liebau, S., Klingenstein, M., Ludolph, A.C., Dengler, R., Kim, K.-S., Hermann, A., Wegner, F., Petri, S., 2016. 4-Aminopyridine induced activity rescues hypoexcitable motor neurons from amyotrophic lateral sclerosis patient-derived induced pluripotent stem cells. Stem Cells 34, 1563–1575. https://doi.org/10.1002/stem.2354.
Nichterwitz, S., Chen, G., Aguila Benitez, J., Yilmaz, M., Storvall, H., Cao, M., Sandberg, R., Deng, Q., Hedlund, E., 2016. Laser capture microscopy coupled with Smart-seq2 for precise spatial transcriptomic profiling. Nat. Commun. 7, 12139. https://doi.org/10.1038/ncomms12139.
Nijssen, J., Aguila, J., Hoogstraaten, R., Kee, N., Hedlund, E., 2018. Axon-Seq decodes the motor axon transcriptome and its modulation in response to ALS. Stem Cell Rep. 11, 1565–1578. https://doi.org/10.1016/j.stemcr.2018.11.005.
Penttilä, S., Jokela, M., Bouquin, H., Saukkonen, A.M., Toivanen, J., Udd, B., 2015. Late onset spinal motor neuronopathy is caused by mutation in CHCHD10. Ann. Neurol. 77, 163–172. https://doi.org/10.1002/ana.24319.
Penttilä, S., Jokela, M., Saukkonen, A.M., Toivanen, J., Palmio, J., Lähdesmäki, J., Sandell, S., Shcherbii, M., Auranen, M., Ylikallio, E., Tyynismaa, H., Udd, B., 2017. CHCHD10 mutations and motor neuron disease: the distribution in Finnish patients. J. Neurol. Neurosurg. Psychiatry 88, 272–277. https://doi.org/10.1136/jnnp-2016-314154.
Picchiarelli, G., Demestre, M., Zuko, A., Been, M., Higelin, J., Dieterlé, S., Goy, M.-A., Mallik, M., Sellier, C., Scekic-Zahirovic, J., Zhang, L., Rosenbohm, A., Sijlmans, C., Aly, A., Mersmann, S., Sanjuan-Ruiz, I., Hübers, A., Messaddeq, N., Wagner, M., van Bakel, N., Boutillier, A.-L., Ludolph, A., Lagier-Tourenne, C., Boeckers, T.M., Dupuis, L., Storkebaum, E., 2019. FUS-mediated regulation of acetylcholine receptor transcription at neuromuscular junctions is compromised in amyotrophic lateral sclerosis. Nat. Neurosci. https://doi.org/10.1038/s41593-019-0498-9.
Prigione, A., Fauler, B., Lurz, R., Lehrach, H., Adjaye, J., 2010. The senescence-related mitochondrial/oxidative stress pathway is repressed in human induced pluripotent stem cells. Stem Cells 28, 721–733. https://doi.org/10.1002/stem.404.
R Core Team, 2019. R: A Language and Environment for Statistical Computing.
Ritchie, M.E., Phipson, B., Wu, D., Hu, Y., Law, C.W., Shi, W., Smyth, G.K., 2015. Limma powers differential expression analyses for RNA-sequencing and microarray studies. Nucleic Acids Res. 43, e47. https://doi.org/10.1093/nar/gkv007.
Rizzo, F., Nizzardo, M., Vashisht, S., Molteni, E., Melzi, V., Taiana, M., Salani, S., Santonicola, P., Di Schiavi, E., Bucchia, M., Bordoni, A., Faravelli, I., Bresolin, N., Comi, G. Pietro, Pozzoli, U., Corti, S., 2019. Key role of SMN/SYNCRIP and RNA-Motif 7 in spinal muscular atrophy: RNA-Seq and motif analysis of human motor neurons. Brain 142, 276–294. https://doi.org/10.1093/brain/awy330.
Saarimäki-Vire, J., Balboa, D., Russell, M.A., Saarikettu, J., Kinnunen, M., Keskitalo, S., Malhi, A., Valensisi, C., Andrus, C., Eurola, S., Grym, H., Ustinov, J., Wartiovaara, K., Hawkins, R.D., Silvennoinen, O., Varjosalo, M., Morgan, N.G., Otonkoski, T., 2017. An activating STAT3 mutation causes neonatal diabetes through premature induction of pancreatic differentiation. Cell Rep. 19, 281–294. https://doi.org/10.1016/J.CELREP.2017.03.055.
Sareen, D., O'Rourke, J.G., Meera, P., Muhammad, A.K.M.G., Grant, S., Simpkinson, M., Bell, S., Carmona, S., Ornelas, L., Sahabian, A., Gendron, T., Petrucelli, L., Baughn, M., Ravits, J., Harms, M.B., Rigo, F., Frank Bennett, C., Otis, T.S., Svendsen, C.N., Baloh, R.H., 2013. Targeting RNA foci in iPSC-derived motor neurons from ALS patients with a C9ORF72 repeat expansion. Sci. Transl. Med. 5. https://doi.org/10.1126/scitranslmed.3007529.
Schindelin, J., Arganda-Carreras, I., Frise, E., Kaynig, V., Longair, M., Pietzsch, T., Preibisch, S., Rueden, C., Saalfeld, S., Schmid, B., Tinevez, J.Y., White, D.J., Hartenstein, V., Eliceiri, K., Tomancak, P., Cardona, A., 2012. Fiji: an open-source platform for biological-image analysis. Nat. Methods. https://doi.org/10.1038/nmeth.2019.
Straub, I.R., Janer, A., Weraarpachai, W., Zinman, L., Robertson, J., Rogaeva, E., Shoubridge, E.A., 2018. Loss of CHCHD10-CHCHD2 complexes required for respiration underlies the pathogenicity of a CHCHD10 mutation in ALS. Hum. Mol. Genet. 27, 178–189. https://doi.org/10.1093/hmg/ddx393.
Sun, W., Maffie, J.K., Lin, L., Petralia, R.S., Rudy, B., Hoffman, D.A., 2011. DPP6 establishes the A-type K+ current gradient critical for the regulation of dendritic excitability in CA1 hippocampal neurons. Neuron 71, 1102–1115. https://doi.org/10.1016/j.neuron.2011.08.008.
The Gene Ontology Consortium, 2018. The gene ontology resource: 20 years and still GOing strong. Nucleic Acids Res. 47, D330–D338. https://doi.org/10.1093/nar/gky1055.
Trokovic, R., Weltner, J., Noisa, P., Raivio, T., Otonkoski, T., 2015. Combined negative effect of donor age and time in culture on the reprogramming efficiency into induced pluripotent stem cells. Stem Cell Res. 15, 254–262. https://doi.org/10.1016/j.scr.2015.05.012.
Vandoorne, T., Veys, K., Guo, W., Sicart, A., Vints, K., Swijsen, A., Moisse, M., Eelen, G., Gounko, N.V., Fumagalli, L., Fazal, R., Germeys, C., Quaegebeur, A., Fendt, S.M., Carmeliet, P., Verfaillie, C., Van Damme, P., Ghesquière, B., De Bock, K., Van Den Bosch, L., 2019. Differentiation but not ALS mutations in FUS rewires motor neuron metabolism. Nat. Commun. 10, 1–12. https://doi.org/10.1038/s41467-019-12099-4.
Wainger, B.J., Kiskinis, E., Mellin, C., Wiskow, O., Han, S.S.W., Sandoe, J., Perez, N.P., Williams, L.A., Lee, S., Boulting, G., Berry, J.D., Brown, R.H., Cudkowicz, M.E., Bean, B.P., Eggan, K., Woolf, C.J., 2014. Intrinsic membrane hyperexcitability of amyotrophic lateral sclerosis patient-derived motor neurons. Cell Rep. 7, 1–11. https://doi.org/10.1016/j.celrep.2014.03.019.
Weltner, J., Balboa, D., Katayama, S., Bespalov, M., Krjutškov, K., Jouhilahti, E.M., Trokovic, R., Kere, J., Otonkoski, T., 2018. Human pluripotent reprogramming with CRISPR activators. Nat. Commun. 9. https://doi.org/10.1038/s41467-018-05067-x.
Wickham, H., 2016. ggplot2: Elegant Graphics for Data Analysis. Springer.
Xiao, Y., Zhang, J., Shu, X., Bai, L., Xu, W., Wang, A., Chen, A., Tu, W.-Y., Wang, J., Zhang, K., Luo, B., Shen, C., 2019. Loss of mitochondrial protein CHCHD10 in skeletal muscle causes neuromuscular junction impairment. Hum. Mol. Genet. https://doi.org/10.1093/hmg/ddz154.
Yu, G., Wang, L.-G., Han, Y., He, Q.-Y., 2012. clusterProfiler: an R package for comparing biological themes among gene clusters. OMICS 16, 284–287. https://doi.org/10.1089/omi.2011.0118.
Zhang, J., Khvorostov, I., Hong, J.S., Oktay, Y., Vergnes, L., Nuebel, E., Wahjudi, P.N., Setoguchi, K., Wang, G., Do, A., Jung, H.J., McCaffery, J.M., Kurland, I.J., Reue, K., Lee, W.N.P., Koehler, C.M., Teitell, M.A., 2011. UCP2 regulates energy metabolism and differentiation potential of human pluripotent stem cells. EMBO J. 30, 4860–4873. https://doi.org/10.1038/emboj.2011.401.
Zhang, J., Nuebel, E., Wisidagama, D.R.R., Setoguchi, K., Hong, J.S., Van Horn, C.M., Imam, S.S., Vergnes, L., Malone, C.S., Koehler, C.M., Teitell, M.A., 2012. Measuring energy metabolism in cultured cells, including human pluripotent stem cells and differentiated cells. Nat. Protoc. 7, 1068–1085. https://doi.org/10.1038/nprot.2012.048.
Zhou, W., Ma, Dongrui, Sun, A.X., Tran, H.-D., Ma, Dong-liang, Singh, B.K., Zhou, J., Zhang, J., Wang, D., Zhao, Y., Yen, P.M., Goh, E., Tan, E.-K., 2018. PD-linked CHCHD2 mutations impair CHCHD10 and MICOS complex leading to mitochondria dysfunction. Hum. Mol. Genet. https://doi.org/10.1093/hmg/ddy413.
Zhu, L., Gomez-Duran, A., Saretzki, G., Jin, S., Tilgner, K., Melguizo-Sanchis, D., Anyfantis, G., Al-Aama, J., Vallier, L., Chinnery, P., Lako, M., Armstrong, L., 2016. The mitochondrial protein CHCHD2 primes the differentiation potential of human induced pluripotent stem cells to neuroectodermal lineages. J. Cell Biol. 215, 187–202. https://doi.org/10.1083/jcb.201601061.